Electric field induced droplet deformation and breakup in confined shear flows

Rattandeep Singh, Supreet Singh Bahga, and Amit Gupta*
Department of Mechanical Engineering, Indian Institute of Technology Delhi, Hauz Khas, New Delhi 110016, India

(Received 12 October 2018; published 6 March 2019)

A numerical investigation of electrohydrodynamics of an initially spherical droplet suspended in a continuous fluid subjected to shear flow in the presence of an electric field is presented. The numerical framework is based on coupling of a multicomponent lattice Boltzmann method with a leaky dielectric model. Simulations reveal distinct deformation and breakup behavior of the droplet for a fixed channel confinement and for widely different viscosity ratio λ. For each λ, defined as ratio of droplet to outer fluid viscosity ($\lambda = \mu_d/\mu_c$), computations are performed for two specific combinations of electrical properties given by ratios of conductivity $R(= \sigma_d/\sigma_c)$ and permittivity $S(= \varepsilon_d/\varepsilon_c)$. Simulations show that the droplet orients toward the direction of shearing motion for $R < S$, whereas it orients along the direction of applied electric field when $R > S$. For $R > S$, the droplet elongation increases with an increase in electric field and breakup of the droplet into smaller droplets is observed beyond a threshold value. The application of electric field also results in the breakup of highly viscous droplets which otherwise are very difficult to break in shear flows. In contrast, the droplet elongation for $R < S$ is observed to be dependent upon the competing interplay of electric and shear stresses acting at the droplet interface. The cumulative effect of electric field and shear flow alters the shear stress acting at the droplet interface, thereby leading to a deviation in the droplet dynamics when $R < S$.

DOI: 10.1103/PhysRevFluids.4.033701

I. INTRODUCTION

In the past decade, microfluidic technologies have evolved rapidly and have found applications in systems including food processing, pharmaceuticals, and material synthesis [1]. The processing of these systems in a microfluidics platform involves deformation, breakup, or coalescence of droplets in a confined flow configuration. The mechanical properties and rheology of the resulting system are governed by the size and morphology of droplets and can be further elevated by an improved understanding of droplet dynamics in confined flow configuration. While actual cases are exceedingly intricate, the study of a single droplet has been considered as a fundamental problem and can provide better insight into the factors involved in more complex cases.

Deformation or breakup of a droplet due to shear flow imposed by two plates moving in opposite directions has been extensively studied and reviewed in the literature [2–6]. In the classical problem analyzed by Taylor [2,6], a droplet of radius a, suspended in another immiscible fluid in an unconfined domain, on the application of shear flow to the continuous fluid was shown to either deform into an ellipsoidal shape with its major axis inclined at an angle with the flow direction or break into smaller droplets. The deformation induced in the droplet was expressed as

$$D = \frac{19\lambda + 16}{16\lambda + 16}\mathrm{Ca}, \tag{1}$$

*agupta@mech.iitd.ac.in

where $\mathrm{Ca} = \alpha a \mu_c / \gamma$ is the capillary number and $\lambda = \mu_d / \mu_c$ is the viscosity ratio. Here $\alpha = 2u/H$ is the shear rate, H is the distance between the plates, γ is the interfacial tension, and μ is the dynamic viscosity. Subscripts c and d denote the continuous fluid and droplet, respectively. Further, Taylor [6] experimentally observed that above a threshold value of capillary number (critical capillary number, $\mathrm{Ca}_{\mathrm{crit}}$) the droplet breaks up. The critical capillary number is a function of the viscosity ratio and the relationship between $\mathrm{Ca}_{\mathrm{crit}}$ and λ was analyzed experimentally by Grace [3]. As the separation H between the two moving wall decreases, the droplet dynamics is also governed by the confinement ratio $\zeta = 2a/H$ besides Ca and λ [7]. Confinement can result in the formation of highly elongated steady droplet shapes, which otherwise would be unstable in an unconfined domain [8]. Further, confinement promotes breakup of droplets when $\lambda > 4$ and inhibits breakup for $\lambda < 1$ scenarios [9,10]. For $\lambda = 1$, $\mathrm{Ca}_{\mathrm{crit}}$ approaches a minima at $\zeta = 0.5$ and any further increase in the confinement results in an increase in the critical capillary number [10].

Manipulation of droplets can be also achieved by the application of an electric field [11–18], where the difference in electrical properties of the droplet and continuous fluid lead to an electric stress at the droplet interface [12]. The magnitude of the electric stress acting on the droplet interface depends strongly on the electric conductivity and dielectric permittivity of the fluids. If the droplet is a perfect conductor or a perfect dielectric liquid and the outer fluid is considered to be a perfect insulator, the application of electric field results in the deformation of the droplet along the direction (prolate) of electric field. In contrast, and as observed experimentally by Allan and Mason [11], a weakly conducting droplet immiscible and immersed in a weakly conducting fluid can deform either along (prolate) or normal (oblate) to the direction of electric field. This fluid behavior was explained by Taylor [14], who identified that weakly conducting (leaky dielectric) fluids can conduct small amounts of charge to the droplet interface. The theoretical predictions [14] and experimental results [17,19] show that for a fixed conductivity ratio $R = \sigma_d / \sigma_c$ and permittivity ratio $S = \varepsilon_d / \varepsilon_c$, the droplet elongation increases with an increase in the electric field strength. Further, experimental [17,19] and numerical [20] analyses show that the droplet no longer attains a quasisteady profile, but rather breaks, depending upon the relative magnitude of R and S beyond a critical electric field. For $R < S$, the droplet stretches across the field direction and breaks into two equally sized droplets [15]. On the other hand, the droplet breaks up either due to end pinching followed by capillary instability or by elongating into a thin thread with formation of several necks along the thread for $R > S$, depending upon the viscosity ratio of the fluids [15,19].

While droplet manipulation using an electric field or shear flow has been the subject of many investigations, the combined effect of electric field and shear flow on a droplet has received very little attention [11,21–23]. The deformation and breakup of a droplet under the combined influence of electric field and shear flow in an unconfined domain was first experimentally analyzed by Allan and Mason [11]. The deformation and orientation induced in the droplet were observed to be dependent upon the strength of shear flow, electric field, and physical properties of the fluids. An analytical solution was proposed by Vlahovska [21] to quantify small deformations induced in a droplet subjected to electric field and shear flow in an unconfined domain. Recently, the effect of electric field on a droplet suspended in a simple shear flow configuration was analyzed analytically by Mandal *et al.* [22], albeit for small deformations only. Numerical simulations were performed by Mählmann and Papageorgiou [23] using the level-set technique to determine the effects of electric field and shear flow on a periodic array of droplets placed in a confined geometry. However, the computations performed were two dimensional in nature.

Thus, an accurate fundamental understanding of three-dimensional droplet behavior in confined flows and subjected to an electric field is still missing in the literature. This analysis of droplet behavior is of significant importance in the realm of microfluidics, where many biofluidic and biomedical applications involve droplet manipulation using an electric field. Motivated by this consideration, in the present work a numerical investigation of a spherical droplet immersed in a confined Couette flow configuration and subjected to a transverse electric field has been carried out. Both the droplet and the continuous media are considered to be leaky dielectric fluids. The numerical simulations are performed by employing a coupled leaky dielectric and multicomponent

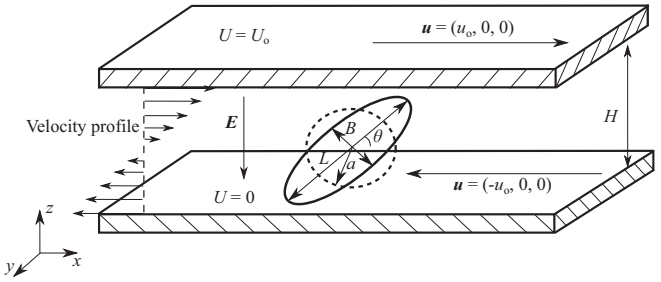

FIG. 1. Schematic of a droplet of initial radius a suspended in a confined Couette flow configuration under the influence of an electric field. The initial droplet profile is represented by a dashed line and the elongated profile is denoted by a solid line. The deformed droplet is oriented at an angle θ with the horizontal direction. The major and minor axes of the droplet are denoted by L and B. The droplet and the outer fluid are assumed to be immiscible and the density of both the fluids is considered to be the same. The top and bottom walls of the domain are separated from each other by a distance H and are moving in the opposite direction. An electric field **E** is acting along the vertical direction.

lattice Boltzmann method [24,25]. Under the combined effect of shear and electric field, the droplet behavior for a wide span of viscosity ratios has been investigated. Further, for a fixed viscosity ratio, the deviations observed in the the droplet behavior for a specific combination of electrical properties $R > S$ and $R < S$ have also been examined. This is the only study that quantitatively captures the three-dimensional deformation and breakup behavior of an initially spherical droplet when immersed in a confined shear flow and subjected to an electric field.

II. MATHEMATICAL FORMULATION

A schematic illustration of a droplet of radius a suspended in a confined Couette flow configuration is shown in Fig. 1. The initial droplet profile is represented by a dashed line and the stretched profile is indicated by a solid line. The major and minor axes of the elongated droplet are denoted by L and B, respectively. The droplet and the continuous fluids are assumed to be immiscible and considered as leaky dielectric fluids. The top and bottom walls of the domain are separated from each other by a distance H and translate along the x direction with velocity $\mathbf{u} = (u_o, 0, 0)$ and $\mathbf{u} = (-u_o, 0, 0)$, respectively. Further, the top wall of the domain is maintained at electric potential $U = U_o$ while the bottom wall is grounded. The electrohydrodynamic behavior of the droplet suspended in a confined shear flow configuration has been analyzed by using a multicomponent low spurious current lattice Boltzmann method coupled with leaky dielectric model [24,25]. A brief outline of the method is described below.

The lattice Boltzmann method (LBM) involves the solution of the discretized Boltzmann equation for the particle distribution function. Within the framework of this model, separate distribution functions are defined for each phase [26]. In the current case, the droplet and the continuous fluids are denoted by two different distribution functions, namely $f_{i,d}$ and $f_{i,c}$, respectively. Using the distribution functions, the macroscopic density of each fluid can be obtained as

$$\rho_k(\mathbf{x}, t) = \sum_i f_{i,k}. \tag{2}$$

Here, subscript k denotes the droplet (d) or outer fluid (c). The droplet and the continuous media are separated from each other by a diffused interface across which the fluid properties undergo a continuous variation. To achieve this, a color function C based on the density of each fluid is

defined, expressed as

$$C(\mathbf{x},t)=\frac{\rho_c(\mathbf{x},t)-\rho_d(\mathbf{x},t)}{\rho_c(\mathbf{x},t)+\rho_d(\mathbf{x},t)}. \tag{3}$$

The value of C varies insignificantly in the pure phase and undergoes a smooth transition across the fluid-fluid interface, thereby creating a diffused region separating the two immiscible fluids. The unit normal vector $\mathbf{n}$ to this diffused interface can be obtained using the gradient of the color function, defined as

$$\mathbf{n}=-\frac{\nabla C}{|\nabla C|}. \tag{4}$$

Since C varies significantly only across the fluid-fluid interface and is nearly constant in the bulk of each fluid, the normal vector $\mathbf{n}$ is calculated at the interface region where the color function is nonzero. This unit normal vector can be further used to determine the local curvature κ of the diffused interface, expressed as

$$\kappa=\frac{1}{R_c}=-\nabla_S\cdot\mathbf{n}, \tag{5}$$

where R_c is the local radius of curvature of the diffused interface and ∇_S is the surface gradient operator [27–29].

In the multicomponent model, the droplet and the continuous fluid undergo collision as a mixed fluid in which the particle distribution function $f_{i,T}(\mathbf{x},t)$ is given as

$$f^t_{i,T}(\mathbf{x},t)=f_{i,c}(\mathbf{x},t)+f_{i,d}(\mathbf{x},t), \tag{6}$$

with the relaxation time as

$$\tau(\mathbf{x},t)=\frac{\tau_c\rho_c(\mathbf{x},t)+\tau_d\rho_d(\mathbf{x},t)}{\rho_c(\mathbf{x},t)+\rho_d(\mathbf{x},t)}. \tag{7}$$

Here τ_d and τ_c are the dimensionless relaxation times [30,31] of the droplet and outer fluid, respectively. The source term incorporating the interfacial force $\mathbf{F}_I$ is incorporated in the collision equation and is given as [32]

$$\Phi_I=w_i\left(1-\frac{1}{2\tau}\right)\left[\frac{\mathbf{e}_i-\mathbf{u}}{c_s^2}+\frac{(\mathbf{e}_i\cdot\mathbf{u})}{c_s^4}\mathbf{e}_i\right]\cdot\mathbf{F}_I, \tag{8}$$

where e_i, u_i, and w_i are the lattice velocity vectors, macroscopic velocity, and weight function [24], respectively. $\mathbf{F}_I$ is the body force term due to interfacial tension, defined as

$$\mathbf{F}_I=-\frac{1}{2R_c}\gamma\nabla C \tag{9}$$

After collision, color segregation step is applied to determine the postcollision distributions of the droplet and continuous fluid, given as [33]

$$f^t_{i,c}=\frac{\rho_c}{\rho_d+\rho_c}f^t_{i,T}+w_i\beta\frac{\rho_c\rho_d}{\rho_c+\rho_d}\cos\theta_f|\mathbf{e}_i|, \tag{10}$$

$$f^t_{i,d}=\frac{\rho_d}{\rho_d+\rho_c}f^t_{i,T}-w_i\beta\frac{\rho_c\rho_d}{\rho_c+\rho_d}\cos\theta_f|\mathbf{e}_i|. \tag{11}$$

Here β is the antidiffusion parameter and is fixed to 0.7 to keep the spurious currents low and maintain a narrow interface thickness [28]. After the color segregation step, each fluid undergoes a streaming operation and the resulting distribution function is used to determine the macroscopic density of each fluid [Eq. (2)].

To model the electrostatic part, the local electrical properties are assumed to vary as

$$\varepsilon(\mathbf{x},t) = \frac{\varepsilon_c\rho_c(\mathbf{x},t) + \varepsilon_d\rho_d(\mathbf{x},t)}{\rho_c(\mathbf{x},t) + \rho_d(\mathbf{x},t)}, \tag{12}$$

$$\sigma(\mathbf{x},t) = \frac{\sigma_c\rho_c(\mathbf{x},t) + \sigma_d\rho_d(\mathbf{x},t)}{\rho_c(\mathbf{x},t) + \rho_d(\mathbf{x},t)}, \tag{13}$$

where ε_d (ε_c) and σ_d (σ_c) are dielectric permittivity and electrical conductivity of the droplet (continuous) fluid. In the presence of an electric field $\mathbf{E}$, the transition of electrical properties at the droplet interface results in an electric stress (Maxwell stress) at the droplet interface, expressed as [34]

$$\underline{\mathbf{T}}^E = \varepsilon\left(\mathbf{EE} - \tfrac{1}{2}E^2\underline{\mathbf{I}}\right). \tag{14}$$

The effect of the electric stress on the droplet interface is also included in the lattice Boltzmann equation by incorporating a source term due to the electric field, expressed as

$$\Phi_E = w_i\left(1 - \frac{1}{2\tau}\right)\left[\frac{\mathbf{e}_i - \mathbf{u}}{c_s^2} + \frac{(\mathbf{e}_i\cdot\mathbf{u})}{c_s^4}\mathbf{e}_i\right]\cdot\mathbf{F}_E, \tag{15}$$

where $\mathbf{F}_E$ is the body force due to electric stress [34]. The inclusion of Φ_E with Φ_I results in the coupling of multicomponent hydrodynamics with dynamics of leaky dielectric fluids.

The electric stress acting on the droplet interface was calculated as follows. The electric field applied on the system is related to the electrical conductivity and free charge density ρ_f by the charge conservation equation [35]

$$\frac{\partial\rho_f}{\partial t} + \nabla\cdot(\rho_f\mathbf{u} + \sigma\mathbf{E}) = 0, \tag{16}$$

where $\rho_f = \nabla\cdot(\varepsilon\mathbf{E})$. Since the charge relaxation timescale is small compared with other timescales, the problem can be assumed to be electrostatic [36]. Equation (16) then can be expressed as

$$\nabla\cdot(\sigma\mathbf{E}) = 0. \tag{17}$$

As electric field in electrostatics is considered to be irrotational, $\mathbf{E}$ can be expressed as

$$\mathbf{E} = -\nabla U. \tag{18}$$

In terms of electric potential, Eq. (17) becomes

$$\nabla\cdot(\sigma\nabla U) = 0. \tag{19}$$

The electric potential distribution in the system is determined by solving Eq. (19) using a finite-difference formulation. The gradients are approximated by using the second-order central differencing scheme at the interior nodes and second-order forward or backward differencing scheme at the boundary nodes of the computational domain. Using the electric potential distribution, the electric field in the system is determined by using Eq. (18).

III. RESULTS AND DISCUSSION

The physical parameters that can influence the electrohydrodynamic behavior of a droplet suspended in confined shear flow can be used to define seven independent dimensionless numbers: capillary number $\mathrm{Ca} = \alpha a\mu_c/\gamma$, Reynolds number $\mathrm{Re} = \alpha a^2\rho/\mu_c$, viscosity ratio $\lambda = \mu_d/\mu_c$, confinement ratio $\zeta = 2a/H$, electric capillary number $\mathrm{Ca}_E = \varepsilon_c E_o^2 a/\gamma$, electrical conductivity ratio $R = \sigma_d/\sigma_c$, and dielectric permittivity ratio $S = \varepsilon_d/\varepsilon_c$. Before analyzing the droplet behavior under the cumulative effect of shear flow and electric field, the individual effects of an electric field and shear flow on a droplet are examined. First, the behavior of a droplet immersed in another

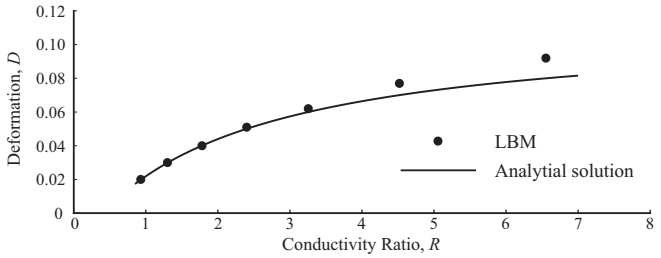

FIG. 2. Comparison of droplet deformation D predicted by the analytical solution of Taylor [14] and our numerical simulations.

immiscible fluid and subjected to an electric field is simulated. Under the influence of an electric field, the droplet deforms either along the electric field (prolate) or orthogonal to the electric field (oblate) [12] depending upon the values of R and S. In the Stokes flow limit, the deformation induced in the droplet can be written as [14]

$$D = \frac{9\mathrm{Ca}_E}{16}\frac{\phi(R,S,\lambda)}{(2+R)^2}, \tag{20}$$

where

$$\phi(R,S,\lambda) = R^2 + 1 - 2S + \frac{3}{5}(R-S)\frac{2+3\lambda}{1+\lambda}, \tag{21}$$

It should be noted that Eq. (20) is applicable only for $D \ll 1$ [12]. In Eq. (21), ϕ is the discriminating function which determines the direction of the droplet deformation [14]. Figure 2 shows a comparison of the droplet deformation D obtained from our simulations and the analytical solution [Eq. (20)] for different values of electrical conductivity ratio while keeping the values of other parameters fixed at $\mathrm{Ca}_E = 0.2$, $S = 0.5$, and $\lambda = 1$. The solid lines in Fig. 2 corresponds to the analytical solution whereas the symbols represent the droplet deformation obtained from the present mathematical model [24,25]. Clearly, deformation induced in the droplet predicted from simulations is in good agreement with the analytical solution. The simulation predictions deviate from the analytical solution when D approaches 0.1, understandably because of the assumption of small deformation ($D \ll 1$) used in deriving the analytical solution. Further validation of the model by varying the interfacial tension and electric field is shown in our previous work [24].

Additionally, droplet deformation D does not vary significantly with change in the viscosity ratio λ, as indicated by Eq. (20). Our simulations correctly predict this behavior with variation of the viscosity ratio. To prove this, we performed simulations for $\lambda = 0.2$, 1 and 5 with $R = 2.4$ and $S = 0.5$. The results obtained are shown in Table I and demonstrate an insignificant variation in deformation parameter D as a function of λ.

Further validation of the model has been carried out by comparing the flow field induced inside and outside of the droplet in the presence of electric field with the analytical solution [13]. The

TABLE I. Comparison of the droplet deformation D obtained using the analytical solution and the mathematical model used in the present work for different viscosity ratios.

λ	D (analytical)	D (numerical)
0.2	0.050	0.051
1	0.050	0.051
5	0.050	0.051

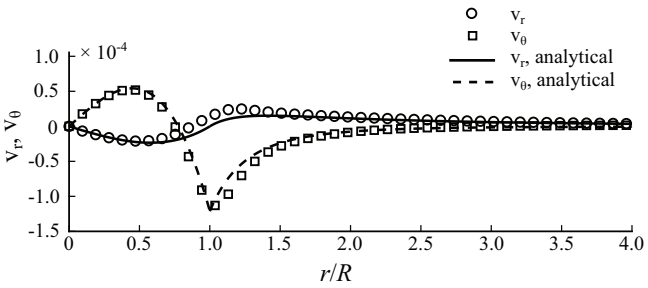

FIG. 3. Comparison of radial and angular velocity components obtained from the present mathematical model and analytical solution for $\theta = \pi/4$.

velocity induced inside and outside the droplet along the polar coordinates r and θ is given by

$$v_r = \begin{cases} A\left(\frac{r}{a}\right)\left[1 - \left(\frac{r}{a}\right)^2\right](3\sin^2\theta - 1) & r \leqslant a, \\ A\left(\frac{a}{r}\right)^2\left[\left(\frac{a}{r}\right)^2 - 1\right](3\sin^2\theta - 1) & r \geqslant a, \end{cases} \tag{22}$$

and

$$v_\theta = \begin{cases} \frac{A}{2}\left[-3\left(\frac{r}{a}\right) + 5\left(\frac{r}{a}\right)^3\right] & r \leqslant a, \\ A\left(\frac{a}{r}\right)^4 & r \geqslant a, \end{cases} \tag{23}$$

where

$$A = \frac{-0.9E_o^2 a\varepsilon_c(R-S)}{(2+R)^2(1+\lambda)\mu_c}. \tag{24}$$

Figure 3 shows a comparison of the velocity field predicted by our model and the analytical solution for $\theta = \pi/4$. The solid and dashed lines in Fig. 3 correspond to the analytical result and the solid symbols represent the values obtained from the present mathematical model. Clearly, the numerically obtained velocity field inside and outside the droplet is in good agreement with the analytical solution.

Next, the deformation and breakup behavior of a droplet suspended in a shear flow configuration in the absence of electric field is examined. As reported in previous experimental and theoretical studies [7,9,10,37,38], the dynamics of a droplet immersed in a confined shear flow configuration is governed by Ca, λ, and $\zeta = 2a/H$. For a fixed value of ζ and λ, the droplet elongation increases with increase in Ca and for $\mathrm{Ca} \geqslant \mathrm{Ca_{crit}}$ the droplet breaks up into smaller droplets. For $\lambda = 1$ and $\zeta = 0.5$, the numerical and experimental analysis performed by Janssen *et al.* [10] indicate that steady ellipsoidal shapes of the droplet were obtained for $\mathrm{Ca} \leqslant 0.35$. A slight variation in the numerical and experimental values of $\mathrm{Ca_{crit}}$ was reported in Ref. [10], where $\mathrm{Ca_{crit}} = 0.37$ and 0.40 were obtained from numerical and experimental investigations, respectively. Numerical analysis performed by Li *et al.* [39] for $\lambda = 1$ and $\zeta = 0.5$ also reported droplet breakup at $\mathrm{Ca} = 0.40$, further implying that $\mathrm{Ca_{crit}} \approx 0.40$ for droplet breakup at $\lambda = 1$ and $\zeta = 0.5$. For $\lambda = 1$ and $\zeta = 0.5$, this deformation and breakup behavior of a droplet is simulated using our multicomponent model. The model is validated by comparing $\mathrm{Ca_{crit}}$ required for the droplet breakup with the value reported in previous studies [40]. The simulations are carried out on a computational domain of size $25a \times 4a \times 4a$. Periodic boundary conditions are applied along the flow and transverse direction. No-slip boundary condition is applied along the top and bottom boundaries of the domain, given as [41]

$$\tilde{f}_i(\mathbf{x}, t + \delta t) = f_{i',t}(\mathbf{x}, t) + 2\frac{\rho w_i}{c_s^2}\mathbf{u} \cdot \mathbf{e}_i, \tag{25}$$

TABLE II. Deformation parameter obtained corresponding to the droplet radius and grid spacing used in grid independence study at Ca = 0.35, Re = 0.1, and $\lambda = 1$.

Description	Droplet radius	Grid resolution	Deformation parameter, D
Mesh 1 (coarse grid)	10	$250 \times 40 \times 40$	0.452
Mesh 2 (regular grid)	15	$375 \times 60 \times 60$	0.483
Mesh 3 (fine grid)	20	$500 \times 80 \times 80$	0.496

where i' is the direction opposite to i. The droplet behavior is examined for Ca = 0.35 and Ca = 0.40 at Re = 0.1. The droplet evolved into an ellipsoidal shape for Ca = 0.35, whereas binary breakup of the droplet is obtained for Ca = 0.40. This suggests that the critical capillary number required for the droplet breakup lies in the range of 0.36 to 0.4, which is in qualitative agreement with the work of Janssen *et al.* [10]. The interface between the drop and the surrounding medium is defined at locations where $C = 0$. To ensure mesh independence of numerical results, a grid sensitivity study is performed by comparing the deformation parameter D obtained at Ca = 0.35 for three different mesh sizes. The deformation parameter is quantified as $D = (L - B)/(L + B)$, where L and B are the length of the major and minor axes of the deformed droplet as shown in Fig. 1. The description of the grid spacing, droplet radius, and the obtained deformation D are given in Table II. As the results obtained using the mesh of $375 \times 60 \times 60$ show good agreement with the fine grid, it is used for further simulations.

Figure 4 shows the evolution of the droplet shape for Ca = 0.35 and Ca = 0.4 at various values of dimensionless time t^*, defined as t/T, where $T = a/u_o$ and u_o is the wall velocity. The sequence of images in Fig. 4(a) shows the evolution of the droplet shape from sphere to a prolate ellipsoid at Ca = 0.35, with the droplet axis inclined at an angle with the flow direction. For Ca = 0.40, the time evolution of the droplet shape is shown in Fig. 4(b). As depicted at time $t^* = t/T = 5$, the application of shear flow leads to the elongation of the droplet. After some time, a waist is formed near the droplet center which contracts continuously with increase in droplet deformation ($t^* = 15$ and 20). The gradual rise in the droplet elongation leads to the development of a neck near the droplet center ($t^* = 26$). The continuous thinning of the neck ($t^* = 28$ and 31) eventually results in

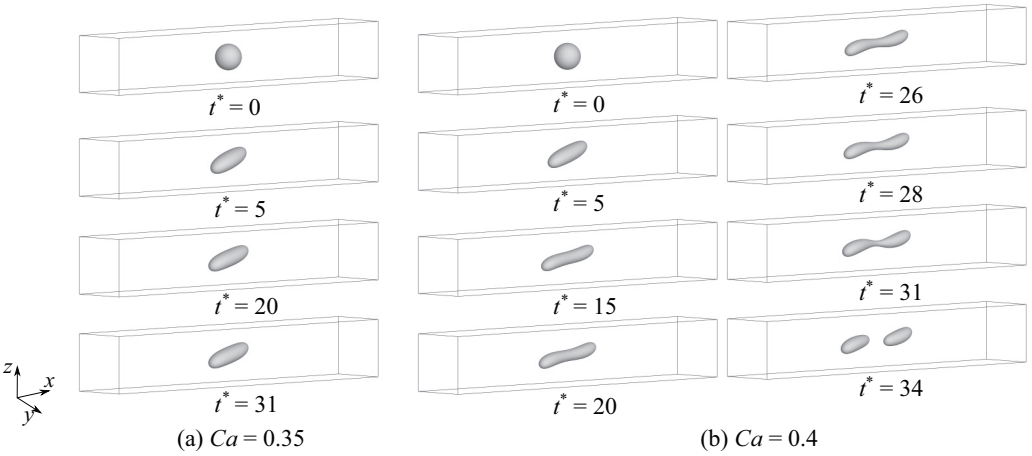

FIG. 4. Shape evolution of a droplet immersed in a confined Couette flow configuration with confinement ratio $\zeta = 0.5$ and Re = 0.1 in a computational domain of size $25a \times 4a \times 4a$. The droplet and the surrounding fluid were assumed to have equal viscosities. For Ca = 0.35, the droplet deforms into a steady ellipsoidal shape with its axis inclined at an angle with the flow direction. The droplet elongates indefinitely in the case of Ca = 0.4, leading to the binary breakup of the droplet.

the breakup of droplet ($t^* = 34$). This evolution of the droplet profile with time at Ca = 0.4 is in quantitative agreement with simulation data available in literature [40].

Subsequently, dynamics of a droplet in a confined shear flow configuration under the influence of an electric field has been analyzed. The size of the computational domain is taken as 375 × 60 × 60 and the droplet radius is considered as 15 lattice units. To apply an electric field **E**, a potential difference between the top and bottom wall of the domain is imposed (as shown in Fig. 1). Two pairs of leaky dielectric fluids with (R, S) as (10,2) (case A) and (0.1, 0.5) (case B) are considered, respectively. Examples of such systems are droplet of castor oil immersed in silicone oil, and vice versa. The experimental values of these oils as reported in Ref. [19] are $R = 10$ and $S = 1.37$ for the analog to case A, and $R = 0.1$ and $S = 0.73$ for that of case B. Simulations are performed for $\lambda = 0.1$, 1, and 10 in order to examine the effect of viscosity ratio on the deformation and breakup behavior of the droplet.

For $\lambda = 1$, Fig. 5 shows the time evolution of droplet deformation and orientation angle corresponding to case A ($R > S$) at Ca = 0.2 and 0.3 for a range of values of $\mathrm{Ca}_E = 0$, 0.1, 0.2, 0.4, and 0.6. The droplet deformation and angle of orientation have been quantified in terms of length of the major axis L and angle of orientation θ as shown in Fig. 1, respectively. As a convention, the initial orientation angle under the influence of shear only (i.e., for $\mathrm{Ca}_E = 0$) is taken as $\pi/4$ [42] with reference to the flow direction. This approach is adopted because the shear stress acting on droplet interface tends to deform a droplet initially into an ellipsoid with its major axis along the direction of strain rate in the absence of an external electric field. To quantify the effect of applied electric field over and above the prevailing shear flow, we follow the same convention of reporting the orientation angle. However, the apparent overshoot only for scenarios with $R > S$ is an artifact due to the assumption that the major axis of the undeformed sphere is oriented at an angle of $\pi/4$ at $t^* = 0$. This overshoot would have not been observed if the initial orientation angle, which can be chosen arbitrarily for a sphere, had been selected as $\pi/2$.

The simulations reveal that the application of electric field leads to an increase in the elongation and orientation of the droplet along the direction of applied electric field. For instance, at Ca = 0.2 and $\mathrm{Ca}_E = 0$ the droplet attains a maximum elongation of $L/2a = 1.36$ and $\theta \approx 30^\circ$, whereas $L/2a$ and θ are 1.42 and 33° for $\mathrm{Ca}_E = 0.1$ at equilibrium, respectively. The droplet elongation and orientation increases monotonically with increase in Ca_E. For a fixed Ca, breakup of the droplet into smaller droplets is observed as $\mathrm{Ca}_E \geqslant \mathrm{Ca}_{E,crit}$. Moreover, $\mathrm{Ca}_{E,crit}$ required for the droplet breakup decreases with increase in Ca. For Ca = 0.2, the droplet breakup occurs at $\mathrm{Ca}_E = 0.4$, whereas for Ca = 0.3 the droplet breakup is observed at $\mathrm{Ca}_E = 0.2$. This behavior is observed to be analogous to that of a droplet placed in shear flow for Re > 1 (in the absence of an electric field), where $\mathrm{Ca}_{\mathrm{crit}}$ for droplet breakup decreases with increase in Re [39,43].

Figure 6 shows the sequence of events in the evolution of the droplet to a steady ellipsoid or breakup into smaller droplets for Ca = 0.3 at $\mathrm{Ca}_E = 0.0$, 0.2, 0.4, and 0.6. Time $t^* = 0$ shows the initial configuration of the droplet subjected to shear flow and electric field. The deformation induced in the droplet can be visualized by comparing the droplet profile for $\mathrm{Ca}_E = 0.0$, 0.2, 0.4, and 0.6 at $t^* = 7$. The simulation results for $\mathrm{Ca}_E = 0$ show that the droplet attains a steady shape over a period of time. In contrast, the droplet is deformed continuously leading to the formation of bulbous ends separated from each other by a thin thread for $\mathrm{Ca}_E = 0.2$, 0.4, and 0.6, with elongation induced in the droplet increasing with Ca_E. Further stretching of the droplet results in the formation of bulbous ends separated from each other by a thin thread. This thinning thread is unstable, eventually leading to the bulbs pinching off to form new droplets as depicted in the last column of Fig. 6. For $\mathrm{Ca}_E = 0.2$, the droplet breakup results in the formation of two daughter droplets, where the original volume of the spherical droplet is equally shared among the resulting droplets. If the original droplet volume is not completely used up by the daughter droplets, the ends of the remaining volume retract either to form a droplet at the center ($\mathrm{Ca}_E = 0.4$) or "bulb up" ($\mathrm{Ca}_E = 0.6$) in a process similar to retractive end pinching [39].

The droplet behavior for $R < S$ (case B) at $\lambda = 1$ is significantly different from that observed when $R > S$ (case A), except that at equilibrium irrespective of R and S the droplet attains a steady

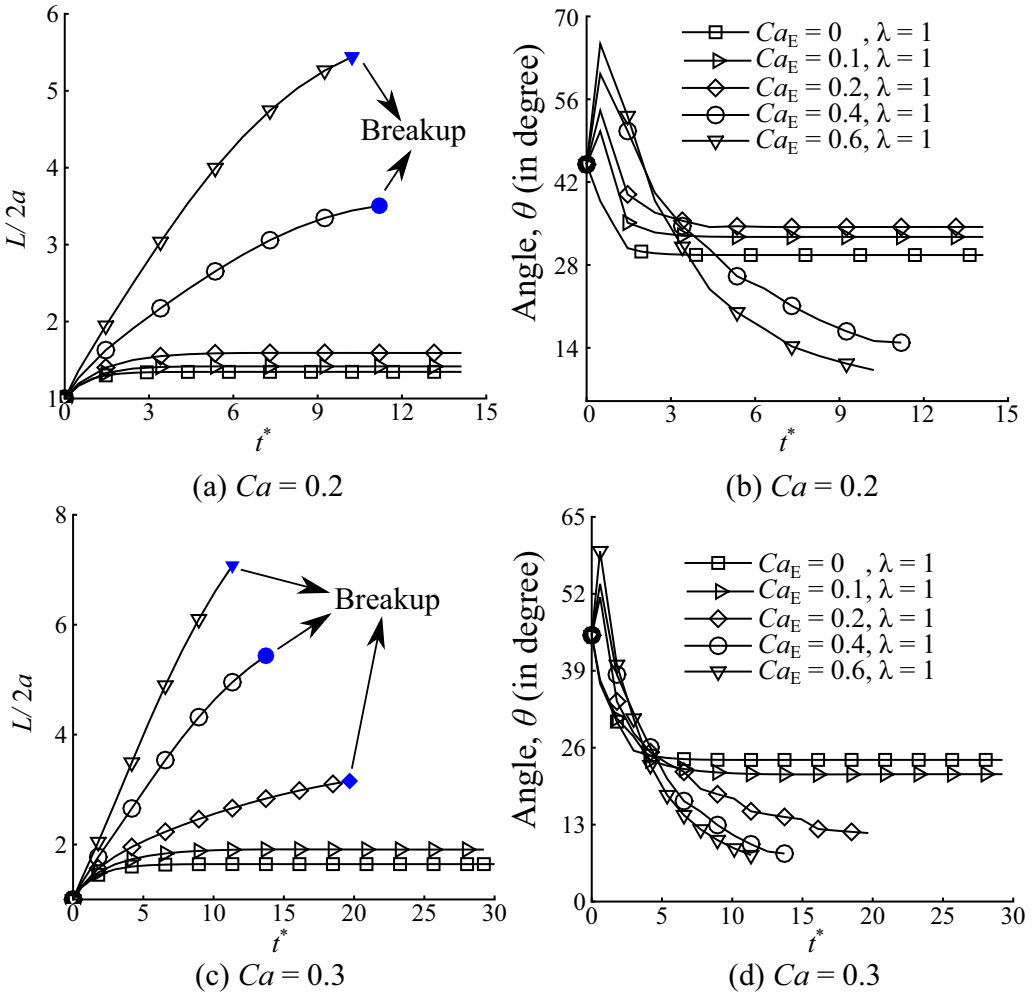

FIG. 5. Evolution of elongation and orientation angle of the droplet corresponding to case A with $R = 10$ and $S = 2$, and $\lambda = 1$ for [(a) and (b)] Ca $= 0.2$ and [(c) and (d)] Ca $= 0.3$ as Ca_E is varied in the range of 0, 0.1, 0.2, 0.4, and 0.6, respectively. Time t has been normalized using $T = a/u_o$, where u_o is the wall velocity. The confinement ratio is considered to be fixed $\zeta = 0.5$. The orientation angle initially increases and after attaining a peak value it decreases. For a fixed Ca, the droplet elongation increases within Ca_E and beyond a critical Ca_E droplet breakup occurs.

prolate ellipsoidal shape inclined at an angle with the shear flow direction. While the orientation angle decreases continuously with Ca_E, the droplet elongation does not change monotonically with Ca_E. The time evolution of the droplet profile obtained by varying Ca_E from 0 to 0.6 for Ca $= 0.2$ and 0.3 is depicted in Fig. 7. The orientation angle for both Ca $= 0.2$ and 0.3 decreases as Ca_E is increased from 0 to 0.1. A further increase in Ca_E leads to a further decrease of the orientation angle, thereby indicating that the droplet orients itself toward the mean flow direction. The elongation induced in the droplet decreases for both Ca $= 0.2$ and 0.3 as Ca_E is increased from 0 to 0.1. For Ca $= 0.2$, a negligible change in the droplet elongation is observed as Ca_E is increased from 0.1 to 0.6, whereas for Ca $= 0.3$ the droplet elongation increases on increasing Ca_E from 0.1 to 0.6. In contrast to case A, no droplet breakup is observed in case B. The steady-state profiles of the droplet obtained for Ca $= 0.2$ and 0.3 at $\mathrm{Ca}_E = 0$ and 0.6 are shown in the inset image of Figs. 7(b) and 7(d).

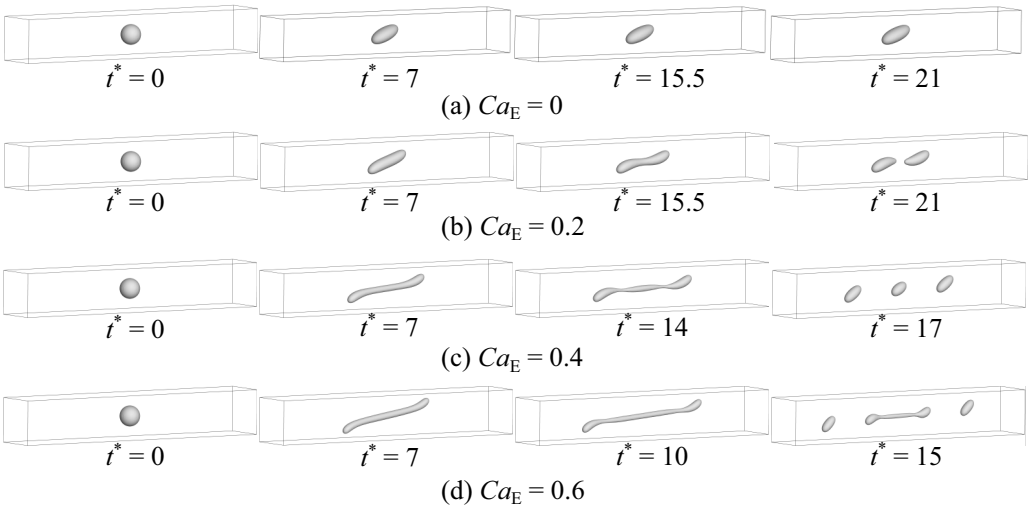

FIG. 6. A sequence of shape evolution of a leaky dielectric droplet at Ca = 0.3 and $\zeta = 0.5$ for (a) Ca_E=0, (b) $Ca_E = 0.2$, (c) $Ca_E = 0.4$, and (d) $Ca_E = 0.6$. The fluids represent case A ($R = 10$ and $S = 2$) and are assumed to have equal viscosities. Figure 6(a) shows the evolution of the droplet into a prolate ellipsoid in the absence of electric field, whereas Fig. 6(b) depicts the breakup of the droplet into smaller droplets at $Ca_E = 0.2$. This indicates that the critical capillary number required for the droplet breakup in the absence of an electric field varies with the application of electric field. With increase in Ca_E, the deformation induced in the droplet increases and the droplet breakup transitions from binary to multiple breakup.

So far, the results in Figs. 5–7 for a fixed Ca indicate that the breakup of a droplet corresponding to case A ($R > S$) can be achieved at lower Ca_E as compared to case B ($R < S$). Further, the mechanism of droplet deformation and breakup in case A is analogous to the behavior of a droplet placed in shear flow with Re > 1 [43]. Next, the viscosity ratio is varied to investigate the effect of applying an electric field in scenarios where viscosities of the two fluids differ substantially.

IV. EFFECT OF VISCOSITY RATIO

The deformation and breakup behavior of a droplet in a confined shear flow configuration is greatly influenced by the relative viscosities of the droplet and continuous fluid [10]. A droplet for $\lambda > 5$ immersed in a shear flow configuration remains nearly spherical and tumbles toward the mean flow direction, thereby making it difficult to achieve droplet breakup. On the other hand, application of shear flow on a droplet for $\lambda < 1$ results in the formation of steady and highly elongated profiles with pointed ends. Compared to $\lambda = 1$, a higher critical capillary number is required for the breakup of a droplet when $\lambda < 1$, whereas it is difficult to achieve breakup of a droplet when $\lambda \geqslant 5$. Depending upon the values of R and S, the behavior of a droplet in a confined shear flow configuration gets altered under the influence of an electric field. We demonstrate this by investigating the cumulative effect of electric field and shear flow on a droplet for $\lambda = 0.1$ and 10 at Ca $= 0.3$ for cases A ($R > S$) and B ($R < S$).

Figure 8 shows the time evolution of deformation and orientation angle of the droplet corresponding to case A for Ca $= 0.3$ at $\lambda = 0.1$ (represented by unfilled symbols) and 10 (represented by filled symbols) for different values of Ca_E. In the absence of electric field ($Ca_E = 0$), the droplet deforms into a steady prolate ellipsoid for both $\lambda = 0.1$ and 10. The change in deformation and orientation angle of the for $\lambda = 10$ under the influence of electric field follows the same trend as depicted in Fig. 5(d) ($\lambda = 1$). A continuous elongation and orientation of the droplet is observed as Ca_E is increased from 0 to 0.2. Further, an increase in Ca_E from 0.2 to 0.425 results in droplet

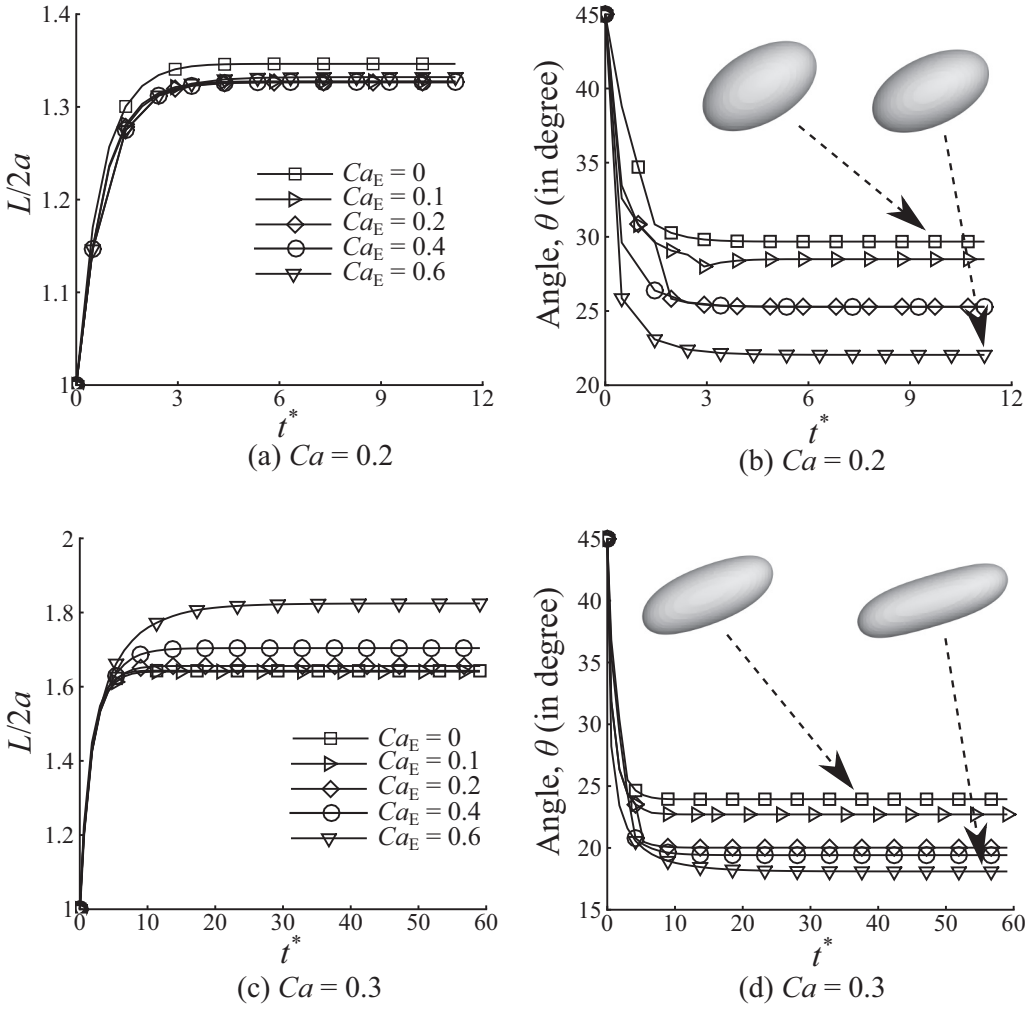

FIG. 7. Evolution of elongation and orientation angle of the droplet corresponding to case B ($R = 0.1$ and $S = 0.5$) for [(a) and (b)] Ca = 0.2 and [(c) and (d)] 0.3, for Ca_E 0, 0.1, 0.2, 0.4, and 0.6, respectively. The fluids are considered to have equal viscosity and the confinement ratio is considered to be fixed, $\zeta = 0.5$. The orientation angle decreases continuously as Ca_E increases. For low values of Ca_E, the droplet elongation decreases with increase in Ca_E. The steady-state droplet profiles for Ca = 0.2 and 0.3 obtained for $Ca_E = 0$ and 0.6 are illustrated in the inset images of Figs. 7(b) and 7(d).

breakup, which otherwise is difficult to obtain in the absence of an electric field. Similar to the results obtained with $\lambda = 10$, deformation and orientation angle for $\lambda = 0.1$ increase as Ca_E is increased from 0 to 0.2. However, a damped oscillatory behavior is observed at $Ca_E = 0.425$ and the droplet breakup occurs at $Ca_E = 0.50$ for $\lambda = 0.1$. This further suggests that, for a fixed Ca, the critical Ca_E required for the droplet breakup is a function of λ. Other than λ, the critical Ca_E required for the droplet breakup also depends upon the confinement ratio. We have highlighted the variation in critical Ca_E with confinement ratio ζ by comparing the droplet behavior in confined and unconfined flows for fluids corresponding to case A ($R > S$) at $\lambda = 0.1$ and 10 in the Appendix.

The transformation of droplet shape for the system with $\lambda = 0.1$ and 10 are shown in Figs. 9 and 10, respectively. For both systems, the time instant $t^* = 0$ represents the initial configuration of the droplet. As shown in Fig. 9, the droplet elongation increases and the droplet evolves from

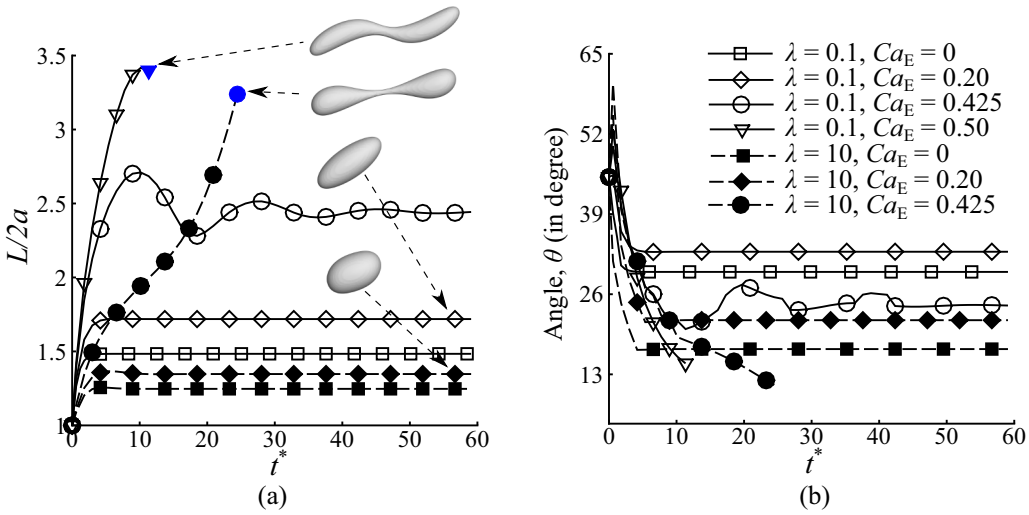

FIG. 8. Effect of viscosity ratio on the (a) deformation and (b) orientation angle of the droplet corresponding to case A ($R > S$) at Ca = 0.3. Highly viscous droplets are denoted by filled symbols, whereas less viscous droplets are represented by unfilled symbols. For $\lambda = 0.1$ and 10, the droplet elongation and rotation toward the transverse direction increase with increase in Ca_E. For $\lambda = 0.1$ and 10, the droplet breakup occurs at $\mathrm{Ca}_E = 0.5$ and 0.425, respectively. The inset image of Fig. 8(a) depicts the droplet profile at steady state and close to droplet breakup for $\lambda = 0.1$ and 10.

rounded to pointed at the extremities with increase in Ca_E for $\lambda = 0.1$. This can be visualized by comparing the droplet profile of $\lambda = 0.1$ for $\mathrm{Ca}_E = 0.2$, 0.425 and 0.50 at $t^* = 6$. While a steady shaped droplet profile is obtained at $\mathrm{Ca}_E = 0.2$, a damped oscillatory behavior is observed for

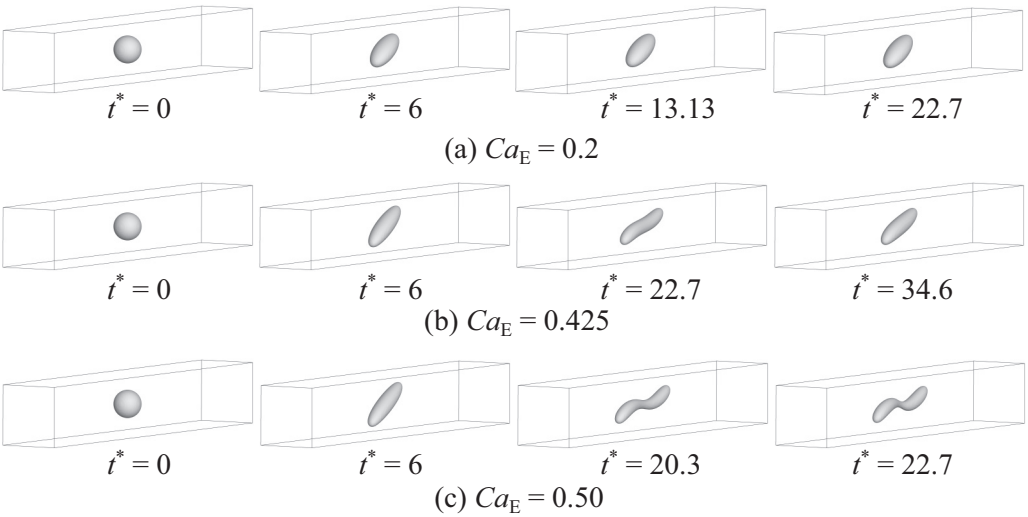

FIG. 9. A sequence of shape evolution of a leaky dielectric droplet at Ca = 0.3, $\lambda = 0.1$, and $\zeta = 0.5$ for Ca_E = (a) 0.2, (b) 0.425, and (c) 0.50. The fluids represent case A where $R > S$ ($R = 10$ and $S = 2$). Figure 9(a) shows the evolution of the droplet shape into a prolate ellipsoid with its major axis inclined at an angle with the flow field direction. At $\mathrm{Ca}_E = 0.425$, the droplet displays a damped oscillatory behavior before attaining a steady shape. Further increase in Ca_E results in the binary breakup of the droplet and indicates a shift in the critical capillary number required for the droplet breakup in the absence of an electric field.

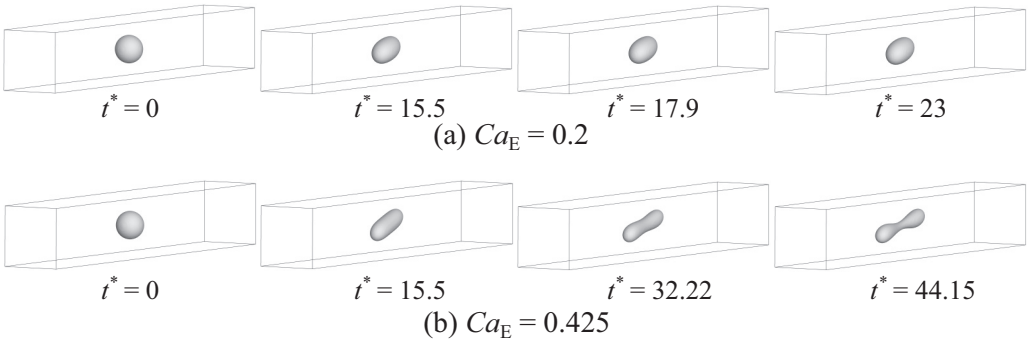

FIG. 10. Interface evolution of a leaky dielectric droplet at Ca = 0.3, $\lambda = 10$, and $\zeta = 0.5$ for Ca_E = (a) 0.2 and (b) 0.425. The fluids corresponds to case *A* where $R > S$ ($R = 10$ and $S = 2$). Figure 10(a) shows the transformation of the droplet shape into a prolate ellipsoid with rounded ends. As Ca_E is increased, the droplet elongation and binary breakup of the droplet occurs at $Ca_E = 0.425$. The breakup of highly viscous droplet at lower value of Ca_E as compared to less viscous droplet (Fig. 9) indicates that it is easier to break highly viscous droplet in a confined geometry under the combined influence of electric field and shear flow than a less viscous droplet.

$Ca_E = 0.425$ [Fig. 9(b)], where the droplet retracts from a sigmoidal shape (at $t^* = 13.13$) to an ellipsoid (at $t^* = 22.7$) before attaining a steady shape. For $Ca_E = 0.50$, the droplet elongates into a sigmoidal shape with the ends separated from each other by a neck. The continuous elongation of the droplet results in the thinning of the neck, thereby resulting in its breakup.

As depicted in Fig. 10 and similar to $\lambda = 0.1$, the droplet deformation increases with Ca_E for $\lambda = 10$. However, and unlike $\lambda = 0.1$, the droplet ends maintain a bulging profile. The increase in droplet deformation with Ca_E can be understood by comparing the droplet profile at $t^* = 15.5$. For $Ca_E = 0.2$, the droplet attains a steady shape, whereas for $Ca_E = 0.425$, a continuous stretching of the droplet is observed, resulting in the formation of two "bulbs" separated from each other by an unstable neck, which eventually breaks and results in the binary breakup of the droplet.

The time evolution of deformation and orientation angle of the droplet corresponding to case B ($R = 0.1$ and $S = 0.5$) for $Ca_E = 0, 0.2, 0.4$ and 0.6 at Ca = 0.3 and $\lambda = 0.1$ and 10 are shown in Fig. 11. The results for $\lambda = 10$ are denoted by filled symbols, whereas the results for $\lambda = 0.1$ are represented by unfilled symbols. The variation in orientation angle with Ca_E for $\lambda = 0.1$ and 10 show a trend similar to the results depicted in Fig. 7(d) ($\lambda = 1$). An increase in Ca_E enhances the alignment of the droplet toward the mean flow direction, thereby reducing the orientation angle of the droplet. The deformation induced in the droplet for $\lambda = 0.1$ and 10 with Ca_E also shows a similar variation as observed in Fig. 7 ($\lambda = 1$). The droplet elongation decreases as Ca_E is increased from 0 to 0.2 and an insignificant change in the droplet elongation is observed as Ca_E is further increased. The steady prolate ellipsoid shaped droplet at $Ca_E = 0.6$ for $\lambda = 0.1$ and 10 are shown as inset images of Fig. 11(a).

We now discuss the three-dimensional features of the drop which are not captured by two-dimensional simulations. In particular, we highlight the evolution of the interface curvature in the plane normal to the direction of flow for three scenarios leading to droplet breakup. Figure 12(a) shows the schematic of the droplet in the plane normal to the direction of flow field (xy plane) at $z = 0$. The solid lines denote the initial shape of the droplet and the dashed lines illustrate the deformed profile of the droplet under the combined influence of electric and shear field.

Here b represents the minor axis of the droplet (neck diameter) in the $z = 0$ plane, which decreases with time as the droplet elongates. Figure 12(b) shows the variation in the nondimensional neck diameter (b/a) with time for $\lambda = 0.1$, 1, and 10 prior to the binary breakup of droplet. As the droplet elongates, the radius of curvature in the $z = 0$ plane increases, thus leading to a decrease in neck diameter with time. Further elongation of the droplet leads to a transition in the curvature

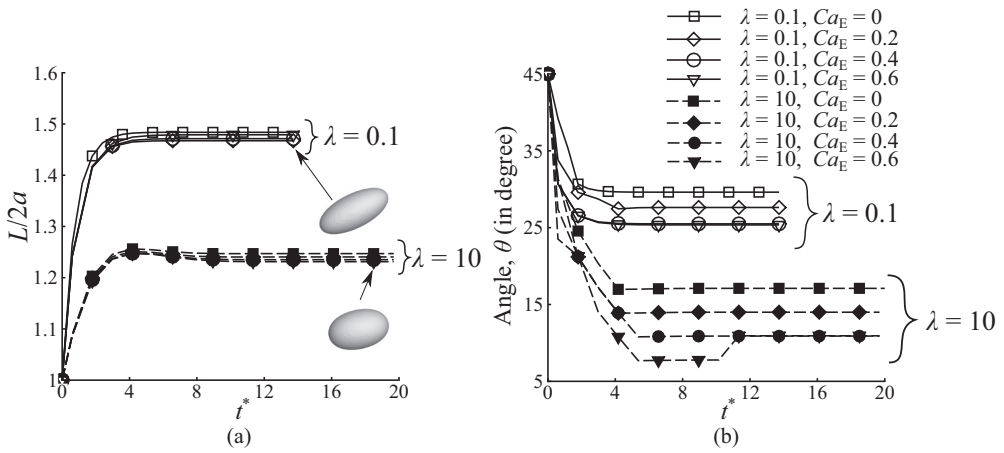

FIG. 11. Effect of viscosity ratio on the (a) deformation and (b) orientation angle of the droplet corresponding to system B at Ca = 0.3. Highly viscous droplets are denoted by filled symbols, whereas less viscous droplet is represented by unfilled symbols. For $\lambda = 0.1$ and 10, the droplet alignment toward the horizontal direction continuously increases with increase in Ca_E. For $\lambda = 0.1$ and low values of Ca_E, the droplet elongation decreases with increase in Ca_E, whereas for $\lambda = 10$ the droplet elongation decreases continuously as Ca_E is increased from 0 to 0.6. The inset image of Fig. 11 depicts the steady-state profiles of the droplet at Ca_E for $\lambda = 0.1$ and 10, respectively.

(concave to convex), resulting in the narrowing of the neck at the droplet center. The variation in b/a with time follows the same pattern for $\lambda = 0.1$, 1, and 10. However, the time required for the

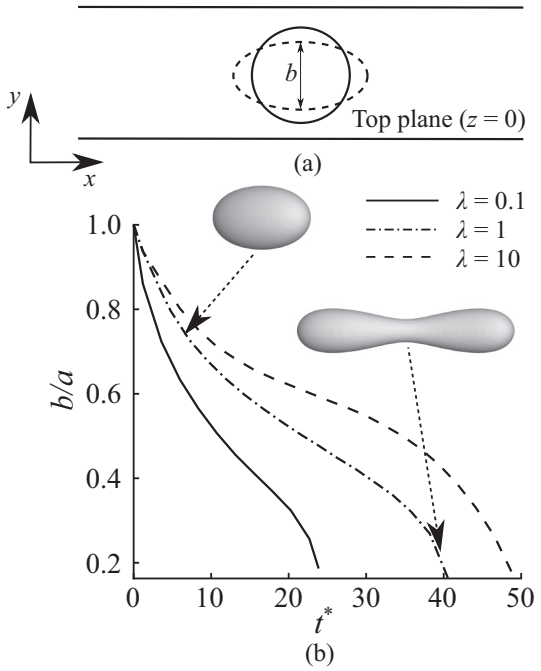

FIG. 12. Effect of curvature on the binary breakup of a droplet along the plane normal to the direction of flow field. Figure 12(a) illustrates the schematic of droplet in xy plane at $z = 0$ and Fig. 12(b) shows the variation in droplets minor axis in $z = 0$ plane with time for $\lambda = 0.1$, 1, and 10.

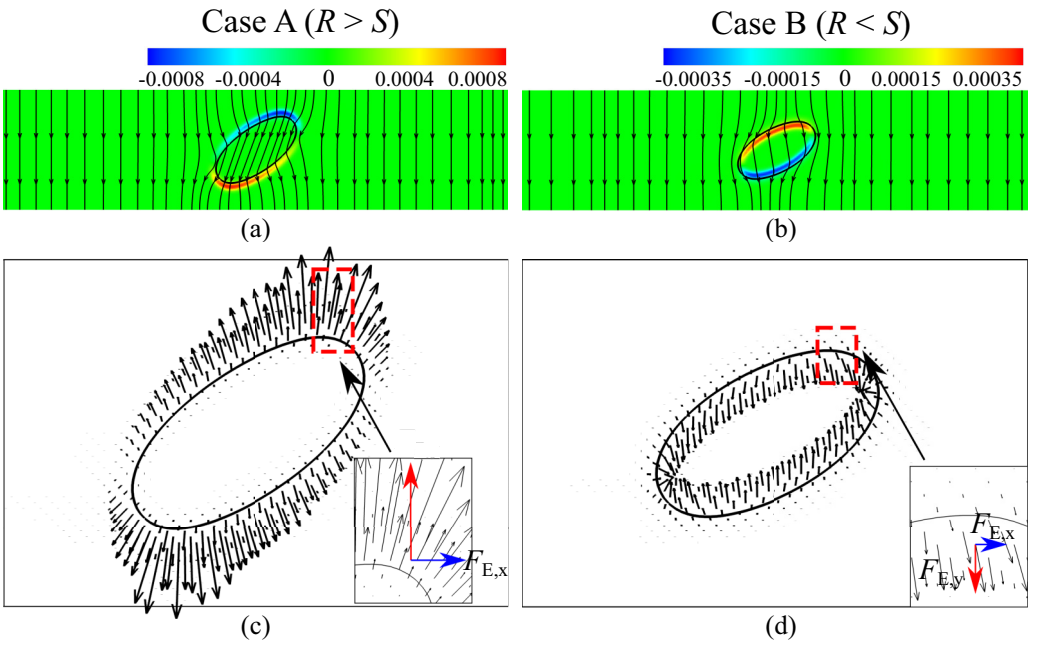

FIG. 13. Charge distribution and the resulting electric force distribution acting on the droplet interface in the presence of an electric field. (a) For case A, the upper (lower) half of the droplet is negatively (positively) charged, causing the electric field lines to converge toward (move away) from the upper (lower) half of the droplet interface. (b) For case B, positive (negative) charge resides on the upper (lower) half of the droplet interface, resulting in the divergence (convergence) of the field lines toward the droplet. [(c) and (d)] The resultant electric force $\mathbf{F}_E$ for case A (B) acts away (toward) the droplet. The inset image highlights that the resultant electric force can be resolved along the vertical $F_{E,y}$ and horizontal component $F_{E,x}$.

breakup of the neck increases with λ. The inset images depict the droplet profiles at different time instance for $\lambda = 1$.

Overall, the following conclusions can be drawn from the deformation and breakup behavior observed in Figs. 5–11. First, irrespective of the viscosity ratio, the droplet corresponding to $R > S$ shows analogous behavior with a droplet placed in shear flows for $\mathrm{Re} > 1$ in the absence of an electric field. Second, the deformation and orientation angle of the droplet corresponding to $R > S$ increases with increase in Ca_E. In contrast, the orientation angle of the droplet corresponding to $R < S$ decreases as Ca_E increases, whereas the droplet elongation varies insignificantly. Lastly, the breakup of a droplet for $\lambda = 10$ corresponding to $R > S$ can be attained under the combined influence of electric field and shear flow, which otherwise are very difficult to break in shear flows ($\mathrm{Ca}_E = 0$). The mechanism explaining the results reported in Figs. 5–11 is now presented.

V. DROPLET DEFORMATION AND BREAKUP MECHANISM

To gain insight into the mechanism of droplet deformation and breakup, the charge distribution and the electric force acting on the droplet corresponding to cases A ($R > S$) and B ($R < S$) are analyzed and shown in Fig. 13. In case A (B), the disparity in electrical properties of the fluids results in the development of negative (positive) and positive (negative) charges at the upper (lower) and lower (upper) halves of the droplet interface, shown in Figs. 13(a) and 13(b). The resulting charge distribution in case A causes the electric field lines to become narrower at the upper and separate out from the lower half of the droplet interface. On the other hand, for case B the electric

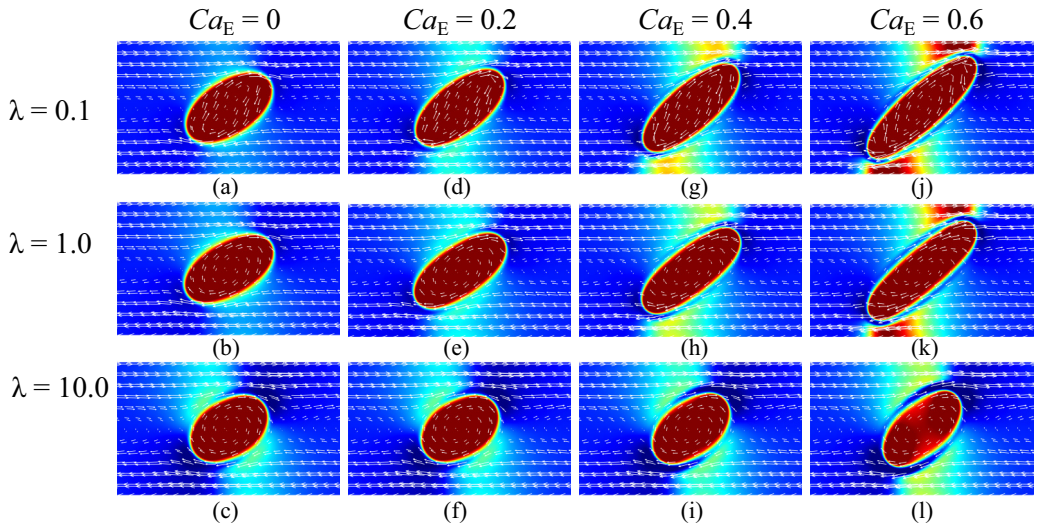

FIG. 14. Velocity vectors and contours of pressure developed in fluids corresponding to system *A* with the variation of Ca_E at Ca = 0.3. For all viscosity ratios, with increase in Ca_E the droplet stretches toward the electrode, leading to an increase of pressure near the droplet ends.

field lines separate out from the upper half and become narrower at the lower half of the droplet interface.

Figures 13(c) and 13(d) illustrate the electric force acting at the droplet interface. In case A, the resultant electric force $\mathbf{F}_E$ points outward, whereas the direction of $\mathbf{F}_E$ is opposite in case B. Owing to the orientation of the droplet, the resultant electric force is decomposed along the vertical ($F_{E,y}$) and horizontal ($F_{E,x}$) directions, as shown in the inset of Figs. 13(c) and 13(d). In case A, $F_{E,y}$ tends to pull the droplet toward the electrode, whereas $F_{E,y}$ in case B pushes the droplet away from the electrode. On the other hand, $F_{E,x}$ in both the case A and case B tends to stretch the droplet toward the mean flow direction.

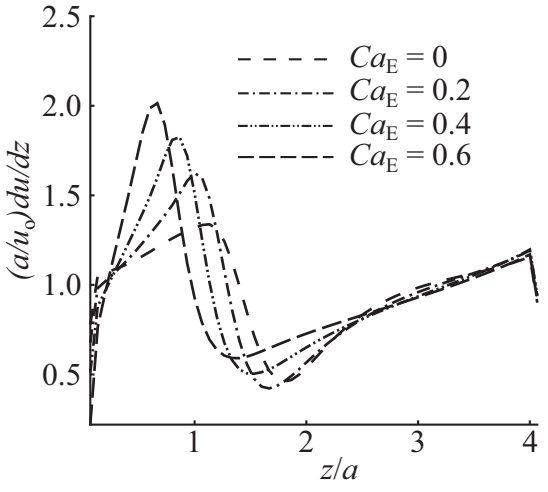

FIG. 15. Variation of shear rate near the droplet poles with increase in Ca_E for $R > S$ at Ca = 0.3 and λ = 1.

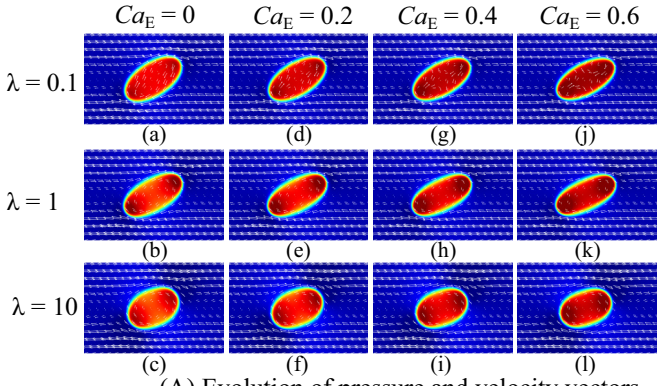

(A) Evolution of pressure and velocity vectors

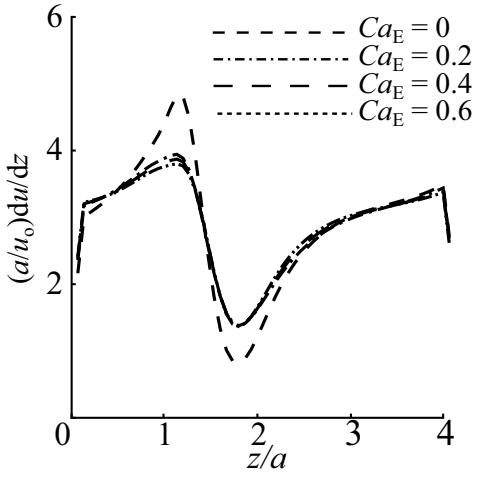

(B) $Ca = 0.3$ and $\lambda = 1$

FIG. 16. Evolution of (A) pressure and velocity vectors and (B) variation of shear rate near the droplet poles at Ca = 0.3 for fluids corresponding to case B ($R < S$) with Ca_E. For all viscosity ratios, with increase in Ca_E the droplet poles orient toward the horizontal direction, thereby leading to an increase in the gap size between the droplet poles and electrode. As a result, negligible pressure build up occurs near the droplet poles. Further, an increase in Ca_E leads to a decrease in shear rate exerted by continuous fluid on the droplet poles with increase in Ca_E.

The physical mechanism for the deformation or breakup of the droplet is explained as follows. In the absence of an electric field, the hydrodynamic forces tend to deform a droplet into a prolate ellipsoid with its axis along with the shear direction. The presence of an electric field modifies the system dynamics depending upon the conductivity and permittivity ratios of the fluids. In the case of fluids with $R > S$ (case A), $F_{E,y}$ pulls the droplet toward the electrode, thereby leading to an increase in the orientation angle of the droplet. This in turn obstructs the flow of continuous fluid, resulting in an increase of pressure near the droplet poles. Figure 14 illustrates the pressure induced in the continuous fluid for Ca = 0.3 at $Ca_E = 0, 0.2, 0.4,$ and 0.6, respectively. For all the viscosity ratios, it is evident that the area for the continuous fluid to pass through between the droplet poles and the electrode decreases as Ca_E increases, resulting in an increase of pressure just upstream of the droplet poles. This buildup of pressure forces the droplet to orient away from the electrode. Further, as illustrated by the velocity vectors in Fig. 14, regions of high velocity are created in the area between the droplet ends and electrode with increase in the droplet elongation.

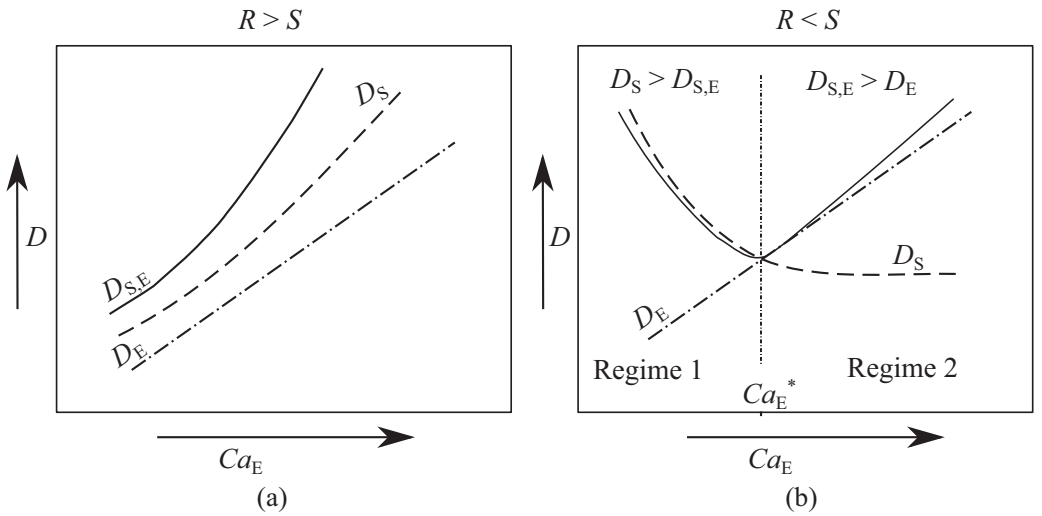

FIG. 17. Schematic illustration of the effective deformation induced in the droplet under the combined influence of electric field and shear flow for (a) $R > S$ and (b) $R < S$.

This suggests that the shear rate near the droplet pole increases with increase in Ca_E. To support this, a comparison of nondimensional shear rate $(a/u_o)du/dz$ versus z/a near the lower bottom of the droplet pole corresponding to $\mathrm{Ca}_E = 0, 0.2, 0.4$, and 0.6 at $\mathrm{Ca} = 0.3$ is presented in Fig. 15. As shown, the shear rate increases as Ca_E increases and shows variation over a narrow zone. Thus, an increase in Ca_E in turn increases the shear force acting on the droplet interface, thereby leading to the increase in stretching of the droplet along the flow direction. This resulting interplay of electric and hydrodynamic forces (comprising pressure, interfacial, and viscous forces) acting on the droplet interface eventually leads to an equilibrium shape or breakup of the droplet.

For $R < S$ (case B), the vertical component of electric force $F_{E,y}$ pushes the droplet away from the electrodes. As a result, the droplet aligns itself toward the mean flow direction. Unlike case A, with increase in the strength of electric field the droplet poles move away from the electrodes, resulting in negligible pressure build. For $R < S$, Fig. 16(a) illustrates the pressure variation near the droplet interface at $\mathrm{Ca} = 0.3$ and $\lambda = 0.1$, 1, and 10, by varying Ca_E from 0 to 0.6. Further, the decrease in orientation angle of the droplet aligns the droplet poles in the region of low velocity. This suggests that in case B the shear rate of continuous fluid near the droplet poles decreases with increase in Ca_E for all the viscosity ratios. As an illustration, the variation of nondimensional shear rate $(a/u_o)du/dz$ versus z/a for $\mathrm{Ca} = 0.3$ and $\mathrm{Ca}_E = 0, 0.2, 0.4$, and 0.6 at $\lambda = 1$ is depicted in Fig. 16(b). As shown, the shear rate decreases as Ca_E is increased from 0 to 0.2 and any further increase in Ca_E leads to a negligible change in the shear rate. Thus, an increase in Ca_E reduces the shear force and enhances $F_{E,x}$ acting on the droplet interface. This competing effect of shear and electric stresses acting on the droplet interface results in an equilibrium shape of the droplet.

VI. GENERALIZED DROPLET BEHAVIOR

A generalized explanation describing the deformation of droplet under the cumulative effect of electric and hydrodynamic force on the droplet elongation for $R > S$ and $R < S$ is illustrated in Fig. 17. The deformation induced in the droplet due to shear stress is represented by D_S and deformation due to electric stress is denoted by D_E. As shown in Fig. 15, the shear rate at the droplet interface for $R > S$ increases with Ca_E. Thus, in the case of $R > S$ for a fixed Ca, the combined action of electric and shear force always increases $D_{S,E}$, as illustrated in Fig. 17(a). For $R < S$, the shear rate at the droplet interface decreases with an increase in Ca_E and beyond

a certain value of Ca_E (Ca_E^*) the change in shear rate becomes insignificant [Fig. 16(b)]. Therefore, the cumulative effect of shear and electric stress on the droplet deformation for $R < S$ is classified into two regimes, as shown in Fig. 17(b). For $Ca_E < Ca_E^*$ (regime 1), D_S varies inversely with Ca_E and the cumulative effect of D_S and D_E leads to $D_{S,E} < D_S$. As Ca_E approaches Ca_E^*, the decrease in D_S is counterbalanced by the increase in D_E, thereby leading to an insignificant change in $D_{S,E}$. In regime 2 ($Ca_E > Ca_E^*$), D_S is a weak function of Ca_E, where a negligible change in D_S occurs with an increase in Ca_E. Hence, the effective droplet elongation $D_{S,E}$ in regime 2 is governed by D_E, which rises as Ca_E increases.

VII. CONCLUSIONS

In this paper, the deformation and breakup behavior of a leaky dielectric droplet immersed in a confined shear flow and subjected to an electric field has been reported. A three-dimensional coupled leaky dielectric multicomponent lattice Boltzmann method has been employed to perform simulations. For a fixed channel confinement and widely different viscosity ratios, the electrohydrodynamic behavior of the droplet was examined for two different combinations of electrical properties, $R > S$ and $R < S$. For $R > S$, irrespective of the viscosity ratio, the application of electric field increases the deformation and orientation of the droplet toward the direction of applied electric field. The increase in orientation angle of the droplet is in agreement with the experimental observations of Allan and Mason [11], which showed that the droplet orientation increases toward the direction of electric field in an unconfined domain. The rotation of the droplet toward the direction of electric field increases the strain rate of the continuous fluid near the droplet poles, thereby leading to an increase in the droplet elongation along the mean flow direction. Further, as electric field (Ca_E) was increased beyond a threshold value ($Ca_{E,crit}$), the breakup of droplet into smaller droplets was observed. In particular, the application of electric field leads to the breakup of droplets where $\lambda > 5$, which are otherwise difficult to break in simple shear flows. The threshold value of electric field strength was observed to depend on the capillary number (Ca) and viscosity ratio (λ). Moreover, the deformation and breakup behavior of the droplet was observed to be analogous to a droplet placed in shear flow for Reynolds number $Re > 1$.

For $R < S$, the application of electric field results in the rotation of the droplet toward the mean flow direction, leading to a decrease in the orientation angle of the droplet with an increase in Ca_E. Again, these simulation predictions are in agreement with the experimental observations of Allan and Mason [11]. For all viscosity ratios, the application of electric field results in a nonmonotonic variation in the droplet elongation. The elongation induced in the droplet depends upon the competing effects of electric and shear stresses acting at the droplet interface. For each viscosity ratio, below a certain value of Ca_E ($<Ca_E^*$), the cumulative effect of electric and shear stresses results in either reduction or negligible variation in the droplet elongation with electric field. On the other hand, for $Ca_E > Ca_E^*$, the droplet elongation increases with increase in Ca_E.

The critical electric capillary number required for the droplet breakup varies with confinement. The variation of critical electric capillary number with confinement ratio will be pursued in a future study. Further, scenarios where the charge relaxation time is comparable or more than the viscous relaxation time should also be considered and the resulting effect on the droplet behavior needs to be examined.

APPENDIX

The behavior of a droplet suspended in a pure shear flow configuration is significantly influenced by the effect of confinement [8–10]. The increase in confinement inhibits the breakup tendency of a droplet with viscosity less than the surrounding fluid. On the other hand, it promotes breakup of a droplet with viscosity much higher than the outer medium [10]. The effect of confinement on a droplet suspended under the combined influence of an electric field and shear flow are reported here. The simulations were performed for $\lambda = 0.1$ and 10, and the confinement effects were examined

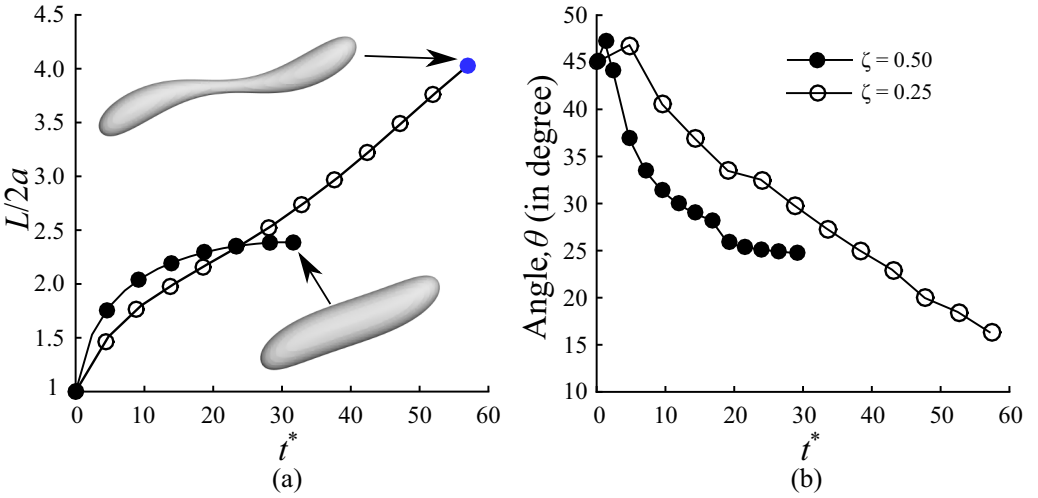

FIG. 18. Effect of confinement on the deformation and orientation induced in a less viscous droplet under the cumulative effect of electric field and shear flow for Ca = 0.3, Ca_E = 0.3, and λ = 0.1. The unconfined domain is denoted by unfilled symbols, whereas the filled symbols represent a confined domain. The inset image depict the steady droplet shape obtained in case of confined geometry and the droplet profile prior to breakup in case of the unconfined domain.

for $\zeta = 0.25$ and 0.50. For the sake of clarity, we refer to the confinement ratio $\zeta = 0.25$ as that corresponding to an unconfined domain, whereas $\zeta = 0.50$ represents a confined domain.

Figure 18 shows the shape evolution and instantaneous orientation angle of the droplet corresponding to $R > S$ (case *A*) for Ca = 0.3 at λ = 0.1 and Ca_E = 0.3. The unfilled symbols denote an unconfined domain ($\zeta = 0.25$) and the confined domain ($\zeta = 0.50$) is depicted by filled

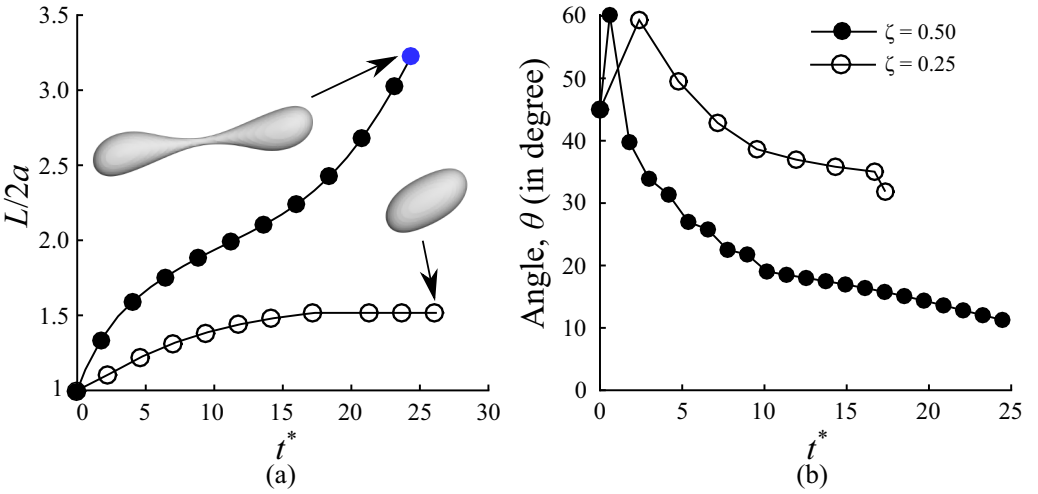

FIG. 19. Effect of confinement on the deformation and orientation induced in a highly viscous droplet under the cumulative effect of electric field and shear flow for Ca = 0.3, Ca_E = 0.425, and λ = 10. The unconfined domain is denoted by unfilled symbols, whereas the filled symbols represent a confined domain. The inset images depict the droplet profile prior to binary breakup obtained in the case of confined geometry and the steady droplet profile obtained in the case of the unconfined domain.

symbols. For $\zeta = 0.50$, the droplet elongation increases with time [Fig. 18(a)] and eventually attains a steady ellipsoidal profile. The results of the droplet orientation for the same scenario are shown in Fig. 18(b) where the droplet orientation initially increases (up to a maximum value) and subsequently decreases. This signifies that the droplet orients along the flow direction before achieving a steady profile. As compared to $\zeta = 0.50$, a significant increase in the droplet elongation is observed for $\zeta = 0.25$. Similarly, after attaining a peak elongation value, the droplet continues to orient along the mean flow direction. The continuous elongation of the droplet results in the formation of a neck at the droplet center, eventually leading to breakup. The inset images in Fig. 18 illustrate the steady droplet shape and droplet profile prior to breakup. This contrasting behavior of the droplet under identical conditions for different confinement ratios suggests that an increase in confinement inhibits breakup when $\lambda < 1$. This observation is also in agreement with the behavior in pure shear flows as mentioned above [10].

Figure 19 shows the time evolution and orientation angle of the droplet corresponding to $R > S$ (case A) for $\mathrm{Ca} = 0.3$ at $\lambda = 10$ and $\mathrm{Ca}_E = 0.425$. Again, the unfilled symbols denote an unconfined domain ($\zeta = 0.25$) and the confined domain ($\zeta = 0.50$) is depicted by filled symbols. For $\zeta = 0.25$, the droplet undergoes continuous elongation [Fig. 19(a)] and attains a steady ellipsoidal profile with its major axis inclined at an angle with the flow field direction. The time evolution of the droplet orientation with the flow field direction is shown in Fig. 19(b). In the case of $\zeta = 0.50$, on the other hand, the droplet undergoes continuous elongation and eventually breaks up into smaller droplets. The opposite behavior in droplet deformation at $\lambda = 10$ for different confinement ratios indicates that the increase in confinement enhances the tendency of the droplet to undergo breakup. This is again in agreement with the results of pure shear flows as mentioned above [10].

[1] R. Dangla, S. C. Kayi, and C. N. Baroud, Droplet microfluidics driven by gradients of confinement, Proc. Natl. Acad. Sci. USA **110**, 853 (2013).

[2] G. I. Taylor, The viscosity of a fluid containing small drops of another fluid, Proc. R. Soc. London, Ser. A **138**, 41 (1932).

[3] H. P. Grace, Dispersion phenomena in high viscosity immiscible fluid systems and application of static mixers as dispersion devices in such systems, Chem. Eng. Commun. **14**, 225 (1982).

[4] H. A. Stone, Dynamics of drop deformation and breakup in viscous fluids, Annu. Rev. Fluid Mech. **26**, 65 (1994).

[5] J. M. Rallison, The deformation of small viscous drops and bubbles in shear flows, Annu. Rev. Fluid Mech. **16**, 45 (1984).

[6] G. I. Taylor, The formation of emulsions in definable fields of flow, Proc. R. Soc. London, Ser. A **146**, 501 (1934).

[7] M. Shapira and S. Haber, Low Reynolds number motion of a droplet in shear flow including wall effects, Int. J. Multiphase Flow **16**, 305 (1990).

[8] V. Sibillo, G. Pasquariello, M. Simeone, V. Cristini, and S. Guido, Drop Deformation in Microconfined Shear Flow, Phys. Rev. Lett. **97**, 054502 (2006).

[9] A. Vananroye, P. Van Puyvelde, and P. Moldenaers, Effect of confinement on droplet breakup in sheared emulsions, Langmuir **22**, 3972 (2006).

[10] P. J. A. Janssen, A. Vananroye, P. Van Puyvelde, P. Moldenaers, and P. D. Anderson, Generalized behavior of the breakup of viscous drops in confinements, J. Rheol. **54**, 1047 (2010).

[11] R. S. Allan and S. G. Mason, Particle behavior in shear and electric fields. I. Deformation and burst of fluid drops, Proc. R. Soc. London, Ser. A **267**, 45 (1962).

[12] D. A. Saville, Electrohydrodynamics: The Taylor-Melcher leaky dielectric model, Annu. Rev. Fluid Mech. **29**, 27 (1997).

[13] J. R. Melcher and G. I. Taylor, Electrohydrodynamics: A review of the role of interfacial shear stresses, Annu. Rev. Fluid Mech. **1**, 111 (1969).

[14] G. I. Taylor, Studies in electrohydrodynamics. I. The circulation produced in a drop by electrical field, Proc. R. Soc. London, Ser. A **291**, 159 (1966).
[15] E. Lac and G. M. Homsy, Axisymmetric deformation and stability of a viscous drop in a steady electric field, J. Fluid Mech. **590**, 239 (2007).
[16] J.-W. Ha and S.-M. Yang, Electrohydrodynamics and electrorotation of a drop with fluid less conductive than that of the ambient fluid, Phys. Fluids **12**, 764 (2000).
[17] S. Torza, R. G. Cox, and S. G. Mason, Electrohydrodynamic deformation and burst of liquid drops, Philos. Trans. R. Soc. London, Ser. A **269**, 295 (1971).
[18] J. Sherwood, Breakup of fluid droplets in electric and magnetic fields, J. Fluid Mech. **188**, 133 (1988).
[19] J.-W. Ha and S.-M. Yang, Deformation and breakup of Newtonian and non-Newtonian conducting drops in an electric field, J. Fluid Mech. **405**, 131 (2000).
[20] W. Du and S. Chaudhuri, A multiphysics model for charged liquid droplet breakup in electric fields, Int. J. Multiphase Flow **90**, 46 (2017).
[21] P. M. Vlahovska, On the rheology of a dilute emulsion in a uniform electric field, J. Fluid Mech. **670**, 481 (2011).
[22] S. Mandal and S. Chakraborty, Effect of uniform electric field on the drop deformation in simple shear flow and emulsion shear rheology, Phys. Fluids **29**, 072109 (2017).
[23] S. Mählmann and D. T. Papageorgiou, Numerical study of electric field effects on the deformation of two-dimensional liquid drops in simple shear flow at arbitrary Reynolds number, J. Fluid Mech. **626**, 367 (2009).
[24] R. Singh, S. S. Bahga, and A. Gupta, Electrohydrodynamics in leaky dielectric fluids using lattice Boltzmann method, Eur. J. Mech. B-Fluid. **74**, 167 (2019).
[25] R. Singh, S. S. Bahga, and A. Gupta, Droplet deformation and breakup due to shear flow and electric field in a confined geometry, in *ASME 2018 16th International Conference on Nanochannels, Microchannels, and Minichannels* (American Society of Mechanical Engineers, Dubrovnik, Croatia, 2018), pp. V001T02A003–V001T02A003.
[26] S. Lishchuk, C. Care, and I. Halliday, Lattice Boltzmann algorithm for surface tension with greatly reduced microcurrents, Phys. Rev. E **67**, 036701 (2003).
[27] A. Gupta and R. Kumar, Flow regime transition at high capillary numbers in a microfluidic T-junction: Viscosity contrast and geometry effect, Phys. Fluids **22**, 122001 (2010).
[28] A. Gupta and R. Kumar, Effect of geometry on droplet formation in the squeezing regime in a microfluidic T-junction, Microfluid. Nanofluidics **8**, 799 (2010).
[29] A. Gupta, H. S. Matharoo, D. Makkar, and R. Kumar, Droplet formation via squeezing mechanism in a microfluidic flow-focusing device, Comput. Fluids **100**, 218 (2014).
[30] S. Chen and G. D. Doolen, Lattice Boltzmann method for fluid flows, Annu. Rev. Fluid Mech. **30**, 329 (1998).
[31] S. Succi, *The Lattice Boltzmann Equation: For Fluid Dynamics and Beyond* (Oxford University Press, Oxford, UK, 2001).
[32] Z. Guo, C. Zheng, and B. Shi, Discrete lattice effects on the forcing term in the lattice Boltzmann method, Phys. Rev. E **65**, 046308 (2002).
[33] M. Latva-Kokko and D. H. Rothman, Diffusion properties of gradient-based lattice Boltzmann models of immiscible fluids, Phys. Rev. E **71**, 056702 (2005).
[34] D. J. Griffiths, *Introduction to Electrodynamics* (Pearson Education, New Jersey, 2005).
[35] A. Ramos, *Electrokinetics and Electrohydrodynamics in Microsystems* (Springer, Berlin, 2011).
[36] R. P. Feynman, in *Feynman Lectures on Physics*, Vol. 2: *Mainly Electromagnetism and Matter*, edited by R. P. Feynman, R. B. Leighton, and M. Sands (Addison-Wesley, Reading, MA, 1964).
[37] M. Minale, A phenomenological model for wall effects on the deformation of an ellipsoidal drop in viscous flow, Rheol. Acta **47**, 667 (2008).
[38] A. Vananroye, P. Van Puyvelde, and P. Moldenaers, Effect of confinement on the steady-state behavior of single droplets during shear flow, J. Rheol. **51**, 139 (2007).
[39] J. Li, Y. Y. Renardy, and M. Renardy, Numerical simulation of breakup of a viscous drop in simple shear flow through a volume-of-fluid method, Phys. Fluids **12**, 269 (2000).

[40] H. Liu, A. J. Valocchi, and Q. Kang, Three-dimensional lattice Boltzmann model for immiscible two-phase flow simulations, Phys. Rev. E **85**, 046309 (2012).
[41] A. J. Ladd, Numerical simulations of particulate suspensions via a discretized Boltzmann equation. Part 1. Theoretical foundation, J. Fluid Mech. **271**, 285 (1994).
[42] P. Janssen and P. Anderson, Boundary-integral method for drop deformation between parallel plates, Phys. Fluids **19**, 043602 (2007).
[43] Y. Y. Renardy and V. Cristini, Effect of inertia on drop breakup under shear, Phys. Fluids **13**, 7 (2001).